steel research international
www.steel-research.de

Crack Initiation Mechanism of AISI 4340 Steel for High-Cycle Torsional Fatigue Loading

Zikuan Xu, Bin Wang, Peng Zhang, Yankun Zhu, Xuegang Wang, and Zhefeng Zhang**

The nucleation of microstructural fatigue cracks in AISI 4340 steel is investigated. The pre-electropolished specimen is employed for the observation of the very early stage of fatigue crack initiation correlated with the microstructure. It is found that there are precipitate-free zones (PFZs) around the lath and packet boundary, and the strength of PFZ is lower than that of the lath due to the lack of second-phase strengthening. Therefore, the fatigue crack would first initiate within the PFZ. Besides, the initiated crack plane usually is the maximum shear stress plane. However, the MnS inclusions would cause stress concentration so that the lath boundary (LB) deviating from the maximum shear stress plane could also have sufficient driving force to crack. In contrast, when the LB is vertical to the cracked MnS inclusion, it would prevent the crack from propagating into the matrix because of the anisotropy of lath martensite. The effects of the stress concentration caused by the MnS inclusion on the maximum deviation angle and the S-N curve are discussed.

1. Introduction

AISI 4340 steel is a low-alloy ultrahigh strength steel, which is mainly used as structural material. Many components made of AISI 4340 steel mainly bear fatigue load, such as the transmission shaft, torsion bar, and crank axle, of which the main failure mode is fatigue fracture.[1–4] For the high-strength steels, the inclusions are the most common sites for fatigue crack initiation, such as nitride,[5–9] oxide,[5,6,8,10–12] and sulfide,[5] represented by TiN, Al_2O_3, and MnS, respectively. Among them, the MnS inclusions are the least dangerous, so the research on its influence on fatigue crack initiation is seldom reported. Recently, the technology of dual vacuum smelting to control the oxygen and nitrogen elements is gradually maturing. The TiN and Al_2O_3 inclusions are effectively eradicated. Therefore, the study on the effect of the MnS inclusions on the fatigue crack initiation is able to carry out.

Except for the inclusion itself, the microstructure of the matrix also needs to be considered. The actual material might be no longer isotropic on the scale of inclusion, such as the lath martensite of the present steel.[13,14] Mine et al.[13] suggested that the block boundaries are an effective grain boundary for impeding dislocation gliding, and the plastic deformation transfer was restricted by the packet boundaries. The lath martensite microstructure in high-strength steels also exhibits anisotropy under fatigue loading.[12,15] Batista et al.[16] proved that lath boundaries are favorable sites for microcrack nucleation. Okada et al.[17] found that incompatibility of plastic strains between adjacent blocks was the origin for the formation of initial fatigue cracks at block boundaries. Therefore, it is necessary for the subsequent model to consider the influence of the inclusion and the microstructure of the matrix at the same time.

However, the fatigue cracking behaviors above only focus on the axial tension-compression fatigue loading in lath martensite materials, while the fatigue cracking induced by torsional fatigue was seldom investigated. Besides, there are indeed some studies on other type of microstructures under torsional fatigue loading, such as the δ ferrite grains in martensitic stainless steel,[18] coarse-grained copper,[19,20] and cast aluminum.[21] Those investigation showed that a different loading-mode condition might result in a different stress state and consequently a different fatigue crack initiation and growth behavior.

In conclusion, the inclusions are the main fatigue crack initiation sites in high-strength steel. Meanwhile, the loading mode and the microstructure of the material might both have effects on the fatigue crack initiation and growth behaviors. In order to clarify that effect, the torsional fatigue tests of AISI 4340 steel were carried out. Mechanisms determining the fatigue crack initiation under torsional fatigue load were studied by revealing microstructural influences and morphologies of early propagating cracks.

2. Experimental Section

The AISI 4340 steel manufactured by vacuum induction melting and vacuum arc remelting was adopted in this study. The elemental compounds are shown in **Table 1**. The bars were cut from the ingot and heated at 850 °C for 1 h then oil quenched followed by 2 h tempering at 204 °C. The ultimate tensile strength of the present steel was 2050 MPa, the yield strength was about 1460 MPa, and the torsional yield strength was about

Z. Xu, B. Wang, P. Zhang, Y. Zhu, X. Wang, Z. Zhang
Shi-changxu Innovation Center for Advanced Materials
Institute of Metal Research
Chinese Academy of Sciences
Shenyang 110016, China
E-mail: pengzhang@imr.ac.cn; zhfzhang@imr.ac.cn

The ORCID identification number(s) for the author(s) of this article can be found under https://doi.org/10.1002/srin.202200976.

DOI: 10.1002/srin.202200976

Table 1. Elemental compositions of the experimental AISI 4340 steel (wt%).

C	Mn	Si	P	[S]	Cr	Ni	Mo	As	Cu	Fe
0.40	0.80	0.28	0.005	0.0027	0.86	1.95	0.26	0.005	0.02	Bal.

932 MPa. Electro-etching was used to reveal the microstructures of fatigue specimens, and the compositions of the etchant were 10% $HClO_4$% and 90% alcohol. A direct-current power supply was used, and the voltage was 12 V. The specimens were etched for 1 min in the etchant at room temperature. The metallography specimen was mechanical polished and followed by etched with 4% nitric alcohol for 10 s. The microstructure images were taken by Zeiss Sigma 500 scanning electron microscope (SEM). The electron gun voltage was 20, and the working distance was about 12 mm.

The torsional fatigue test, using specimens with a gauge section $\Phi 5.5 \times 30\ mm^2$, was carried out on the Instron 8874 system with a stress ratio of $R = -1$, and the loading frequency was in the range of 0.5–19 Hz. Unelectropolished specimens were employed for the S–N curves, and preelectropolished specimens were used for the observation of the very early stage of fatigue crack initiation. All tests were carried out at room temperature. The torsional fatigue fractographies were observed by the Zeiss Sigma 500 SEM.

3. Results

3.1. Microstructures and Inclusions

Figure 1a,b shows the SEM and electron back scattered diffraction (EBSD) images of the matrix microstructures of the present AISI 4340 steel. The steel tempered at 204 °C for 2 h possesses a typical lath martensite microstructure. The clear martensite lath and packet could be seen in Figure 1a,b. In addition, the number of precipitates in the lath varies as shown in Figure 1a. As the fatigue crack initiation site in many reports,[12,15–17] the lath boundary (LB) and packet boundary (PB) were carefully observed. The high magnification image of the LB is displayed in Figure 1c. Numerous precipitates are precipitated in the lath, while there are PFZ on both sides of the LB. Figure 1d exhibits the high magnification image of the PB, and there are also PFZ around the PB. In addition, the size of the precipitate is relatively small compared to Figure 1c. The PFZ around boundary might be due to that the carbides precipitated along the boundary, including the LB and PB, consume too much carbon elements. This phenomenon is also common in maraging steels,[22–25] titanium alloys,[26,27] and aluminum alloys,[28] and the PFZ is also the fatigue crack initiation origin in the above materials.

Figure 2 displays the SEM images and the composition of the inclusion in the present steel, and the inclusion is MnS analyzed by the energy-dispersive spectroscopy (EDS). Due to the adoption of the vacuum induction melting and vacuum arc remelting process, the oxygen and nitrogen elements are well controlled so that inclusions, such as Al_2O_3 and TiN, are not observed, which are claimed to be more negative to fatigue performance than MnS inclusions.[29,30]

3.2. Torsional Fatigue Properties

Figure 3 shows the relationship between the shear stress amplitude and the fatigue life at failure of the present steel, and the

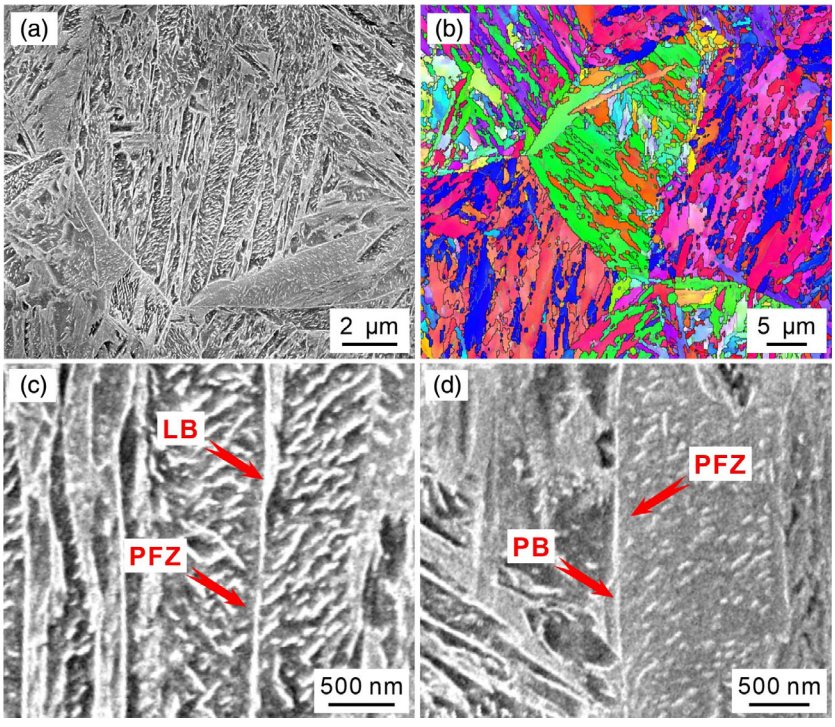

Figure 1. The images of microstructure of AISI 4340 steel tempered at 204 °C for 2 h. a) SEM and b) EBSD, and high magnification of c) lath boundary and d) packet boundary.

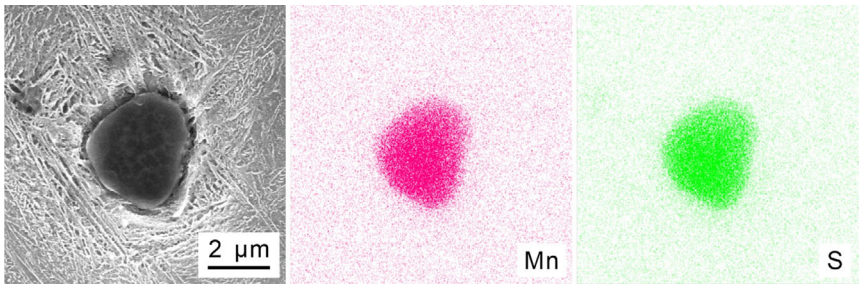

Figure 2. The MnS inclusions and the EDS analysis.

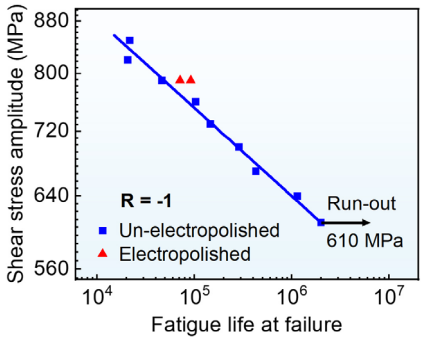

Figure 3. The relationship between the shear stress amplitude and the fatigue life at failure for the fatigue-electropolish specimen.[41]

data show low dispersion. The fatigue life of the specimen at stress amplitude of 610 MPa exceeded 2×10^6 cycles. The fatigue life of pre-electropolished specimens surpass the unelectropolished specimens in a minor advantage.

The most common torsional fatigue fracture for the present steel is displayed in **Figure 4**a. The high magnification image of the fatigue crack initiation site is shown in Figure 4b. The initiation sites of the main crack of all the specimens were carefully examined, and no inclusions were found, which may be due to the inclusion falling off after long cycles at low stress amplitude and extrusion deformation of final fracture. The low and high magnifications of the side views of the fatigue crack initiation site are presented in Figure 4c,d, respectively. The crack initiates along the maximum shear stress plane. After growth in mode II for a short distance, the crack branches off into two cracks about 45° to the specimen axis. The length of mode II crack path is in range of 30 to 50 μm for the fractures.

3.3. Initiation Behaviors Without MnS Inclusion

To reveal the fatigue crack initiation mechanism, pre-electropolished specimens are employed to observe the

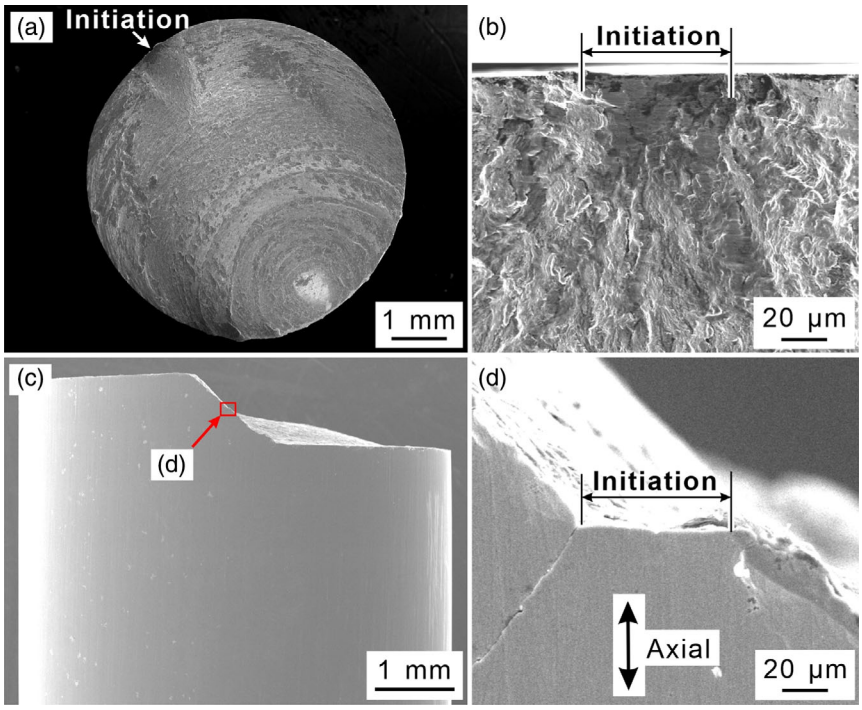

Figure 4. The SEM images of the fracture morphologies of pure torsional fatigue specimens. a) Typical fracture. b) The initiation site is marked.[41] c) The side view of the initiation site. d) High magnification of the initiation site marked in (c).

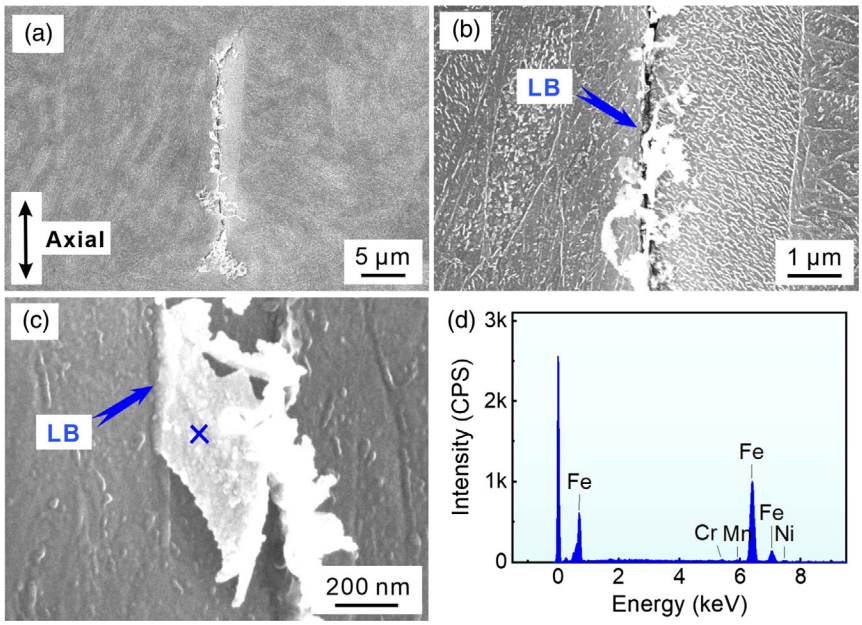

Figure 5. The fatigue crack initiation without MnS inclusion. a,b) The initiated crack in lath boundary. c) The extrusion morphology in lath boundary. d) EDS results of the mark in (c).

relationship between the initiated fatigue crack and the microstructure. **Figure 5**a–c shows the SEM images of the pre-electropolished specimen after fatigue test. The fatigue crack initiated from the lath martensite boundary and the direction of the LB is the same as the specimen axis, which is the maximum shear stress plane caused by the external loading. There are many matters on the crack surface, and the high magnification image is shown in Figure 5c. It is tongue like and is squeezed out from the LB. After EDS analysis is shown in Figure 5d, it is found that the component of the tongue-like matter is the same as the material itself. This is a typical extrusion morphology, which is one of the most important fatigue damage mechanisms.[31–33] This indicates that there is weak region around the LB, and cumulative plastic deformation would occur during the cyclic loading.

3.4. Initiation Behaviors with MnS Incluison

The appearance of MnS inclusion certainly affects the fatigue crack initiation behavior. The MnS inclusion itself would crack in maximum shear stress plane under the cyclic loading, as shown in **Figure 6**. After carefully observation, it is found that the direction of the crack and the lath around the crack tip is different, and the lath is almost perpendicular to the crack. It is well known that the crack prefers to grow in shear mode in the early stage.[34–36] In the present steel, the crack also prefers to grow in the LB. However, when the LB is vertical to the crack, it would block the crack from continuing to propagate into the matrix.

In contrast, when the LB around the MnS inclusion is in the direction of the maximum shear stress plane, the MnS inclusion could lead to the matrix cracking, as shown in **Figure 7**a,b. It is confirmed that the initiated crack is along the LB, as shown in Figure 7c,d. The schematic illustration of relationship between the crack and the microstructure is displayed in Figure 7e.

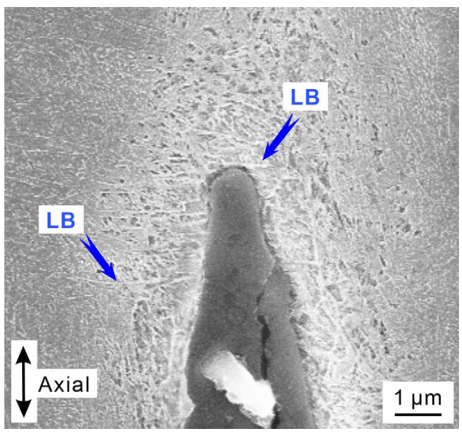

Figure 6. Cracked MnS inclusion. a) SEM. b) Schematic illustration of the relationship between the cracked MnS inclusion and the microstructure.

The MnS inclusion on the LB acts as a stress concentration position and further increases the cracking possibility of the LB. In the meantime, instead of strictly consistent with the maximum shear stress plane, the initiated crack has a deviation of 6°, as shown in Figure 7a.

4. Discussion

Based on the earlier results, it is clear that the final fatigue fracture of the present steel is due to the cracks initiated in the LB. The MnS inclusions are a secondary cause that could affect the cracking behavior of the LB. Therefore, the fatigue crack

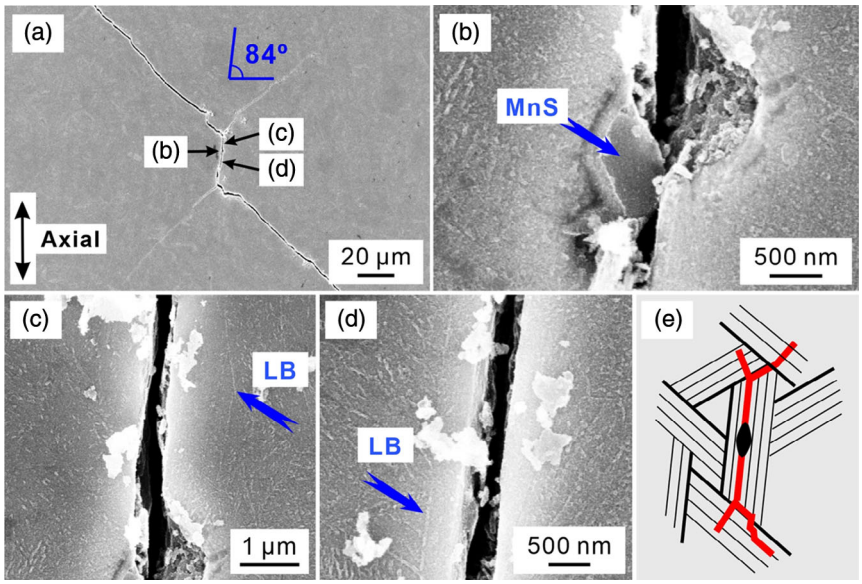

Figure 7. Fatigue crack initiation with MnS inclusion. a) Low magnification. b–d) High magnification. e) Schematic illustration of the relationship between the crack and the microstructure.

initiation mechanism will be discussed in two aspects separately, including without or with the MnS inclusion.

4.1. Fatigue Crack Initiation Without MnS Inclusion

The influencing factors of the LB cracking in maximum shear stress plane can be divided into the microstructure and the external loading.

The PFZ around the LB acts as a weak region. Extrusions around the LB after fatigue test were observed as shown in Figure 5c. Generally, plastic deformation occurs first in the weak region.[31,37–39] Koschella et al.[12] and Seidametova et al.[15] also found exemplary extrusion parallel in the LB. This may be attributed to two factors. First, the martensite lath packet as a whole is anisotropic. Specifically, a packet usually contains several blocks of martensite lath with different orientations. At this time, the strength in the direction of LB is different to the direction perpendicular to the LB. That is because the dislocations in the direction perpendicular to the LB need to pass through the boundary in order to move. Furthermore, the orientation on both sides of the block boundary is different, and the block boundary would produce a similar grain-size strengthening effect. Instead, in the direction of the block boundary, the dislocation movement does not need to pass through the boundary, so the strength will be lower. The conclusions above could be supported by the researches of Morsdorf et al.[14] in the deformation behavior of regular size specimens and Mine et al.[13] of micro-tension specimens. Second, in the direction of the LB, the strength of PFZ around the LB is lower than that of the lath.[25] The lath has plenty of precipitates and dislocations with C atoms absorbed, while the PFZ is lack of precipitate, as schematic illustrated in **Figure 8**.

The maximum shear stress plane formed by the applied load offers the driving force. The direction of the LB is randomly

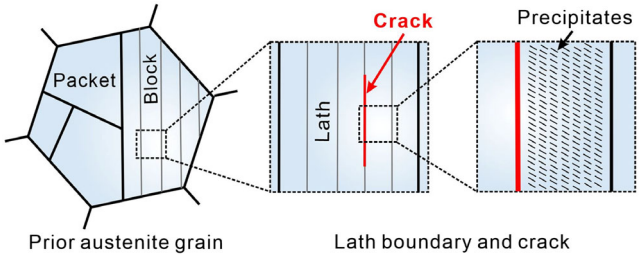

Figure 8. Schematic illustration of fatigue crack initiation at martensite lath without MnS inclusion.

distributed, while the direction of the maximum driving force is fixed. Therefore, only the LB in the direction of the maximum shear stress plane would obtain the maximum driving force and have the maximum possibility of cracking.

4.2. Fatigue Crack Initiation with MnS Inclusion

Without MnS inclusion, the LB needs to be in the maximum shear stress plane. In the same loading, the existence of MnS inclusions allows a slight deviation between the LB and the maximum shear stress plane because of the stress concentration caused by the MnS inclusion, as shown in **Figure 9**. The maximum deviation angle could be quantified. First, the shear stress on an arbitrary plane without the MnS inclusion is conculcated by

$$\tau = \tau_{xy}\cos 2\theta \tag{1}$$

where τ_{xy} is the applied shear stress, and θ is the angle of an arbitrary plane and is represented by the dash line in Figure 9. Second, for an arbitrary plane with MnS inclusion,

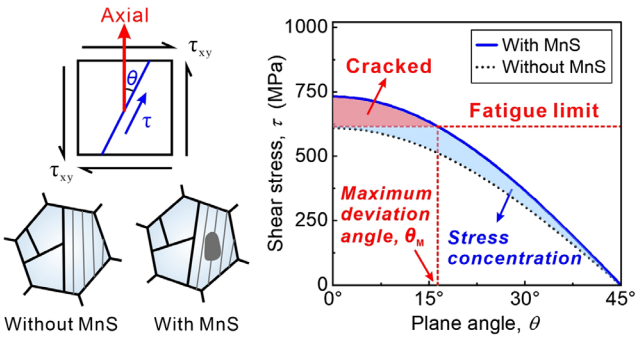

Figure 9. The effects of the local stress concentration caused by the MnS inclusion on the cracking of the LB.

due to the stress concentration effect, the shear stress needs to be multiplied by the stress concentration factor α

$$\tau = \alpha\tau_{xy}\cos 2\theta \tag{2}$$

and is represented by the solid line. The stress concentration factor used in the Figure 9 is 1.2. Due to the stress concentration caused by the MnS inclusion, even when the LB is not in the maximum shear stress plane, the LB would still crack. The maximum deviation angle θ_M between the LB and the maximum shear stress plane is related to the stress concentration factor by the following equation

$$\theta_M = \frac{1}{2}\cos^{-1}\frac{1}{\alpha} \tag{3}$$

The stress concentration factor of MnS inclusion in Figure 7 is simulated by finite element method. The cracking mode in the Figure 7 should be the interface cracking, so a hemispherical pit is used for the simulation. The results of maximum principal stress (σ_1) and minimum principal stress (σ_3) are shown in **Figure 10**a,b, respectively. The external torque surrounds the *X*-axis and generates a shear stress of 100 MPa ($\tau_{External}$) as the reference stress. The shear stress concentration factor is defined as

$$\alpha = \frac{\tau}{\tau_{External}} = \frac{\sigma_1 - \sigma_3}{2\tau_{External}} \tag{4}$$

The stress concentration factors of three typical locations are listed in Figure 10c. Each of the principal stress value listed in Figure 10c is the average value of the four surrounding cells. It is clear that location A has the maximum stress concentration factor, which is about 1.09. Furthermore, location A is in the axis direction, which is consistent with cracking mechanism. Meanwhile, the relationship between maximum deviation angle θ_M and stress concentration factor α given by Equation (3) is shown in Figure 10d. The maximum deviation angle increases with the increase of stress concentration factor. When the angle of the LB is less than the maximum deviation angle, the LB would crack. The angle of the LB and the stress concentration factor of

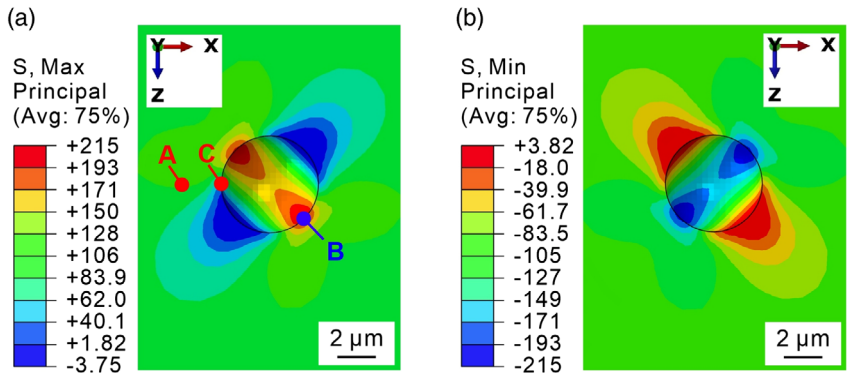

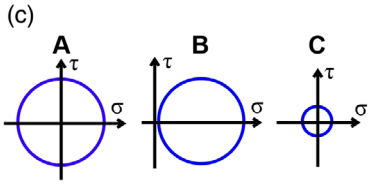

	Principal Max	Principal Min	Stress concentration factor
A	+109	-109	1.090
B	+215	-0.16	1.075
C	+38.2	-38.5	–

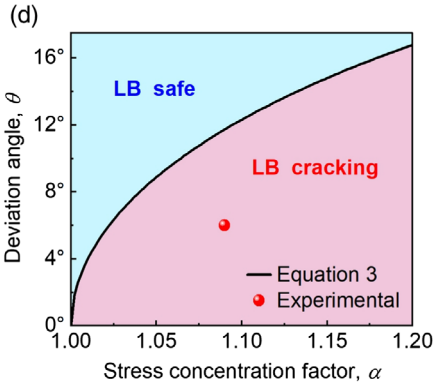

Figure 10. The effect of MnS inclusion on the lath boundary cracking. a) The maximum principal stress and b) the minimum principal stress simulated by the finite element method. c) The schematical illustration of the maximum shear stress in sites A, B, and C marked in (a). d) The relationship between the deviation angle and the stress concentration factor.

the MnS inclusion in Figure 7 are located in the region of LB cracking in Figure 10d, which is consistent with the prediction result of Equation (3).

4.3. Comparation Between Tensile and Torsional Fatigue

The effect of the MnS inclusion on the S-N curve under cyclic shear stress is summarized in **Figure 11**a. The fatigue crack initiates on the specimen surface both with and without the MnS inclusion due to that the maximum stress is on the specimen surface. When there is no MnS inclusion, the PFZ around the LB is the weakest region, and the LB would crack along the maximum shear stress plane. When there is the MnS inclusion, the cracking mechanism remains unchanged except for that the required stress amplitude would decrease due to the stress concentration caused by the MnS inclusion.

However, the size of MnS inclusion could be a critical factor. When the size of MnS inclusion is big enough so that the stress intensity factor caused by the inclusion is beyond the nonpropagating threshold value, the fatigue crack initiation would be no longer dominated by the shear stress but normal stress. The crack initiation mechanism would change from the mode II crack to the mode I crack. In that case, the S-N curve with inclusions would be no longer the downward translation of the S–N curve without inclusions. The stress intensity factor of a inclusion could be calculated using the method proposed by Murakami[40]

$$\Delta K_{\mathrm{inc}} = 0.65\tau_{\mathrm{a}}\sqrt{\pi\sqrt{\mathrm{area}}} \tag{5}$$

The inclusion size corresponding to mechanism transformation could be calculated by

$$d_{\mathrm{c}} = \frac{1}{\pi}\left(\frac{\Delta K_{\mathrm{th}}}{0.65\tau_{\mathrm{a}}}\right)^2 \tag{6}$$

where ΔK_{th} is the threshold value of stress intensity factor, which is about 5.35 MPa $\mathrm{m}^{1/2}$ obtained in our previous study.[41] According to Equation (6), the critical inclusion size is related to the stress amplitude, and the larger the stress amplitude is, the smaller is the corresponding critical inclusion size. The highest loading value in the present study is 850 MPa, and the inclusion size corresponding to mechanism transformation is about 30 μm calculated by Equation (5). This inclusion size is much larger than the observed inclusion size in the present steel.

In addition, when the inclusion size is smaller than 30 μm, the larger the inclusion is, the greater the stress concentration is and the greater the decline of the required stress amplitude would be. However, the required stress amplitude should not decrease continuously because the fatigue crack initiation caused by the inclusion does not necessarily lead to the fatigue failure. If the stress amplitude reduces too much, although the driving force for crack initiation is enough due to the stress concentration caused by inclusion, the driving force for the nonpropagating threshold might not be enough. Furthermore, since the martensitic PB is the first microstructural barrier encountered after the crack initiated in the LB as illustrated in Figure 7e, the stress intensity factor of the crack tip would depend on the packet length and the stress amplitude. Therefore, the specific value of the minimum required stress amplitude should be related to the length of the martensitic packet and independent of the inclusion size. The longer the packet is, the smaller the minimum required stress amplitude is.

Different from the cyclic shear stress, the crack initiation mechanism would change when refers to surface cracking and internal inclusion cracking under cyclic normal stress.[42,43] Therefore, there will be the well-known step-wise S-N curve attributed to different cracking mechanisms, as shown in Figure 11b. The curve in blue refers to the surface-induced fracture, which has a typical fatigue limit. The curve in red refers to the fatigue fracture caused by internal inclusion, and the characteristic of the curve depends on the shape and size of the inclusion.

5. Conclusions

The high-cycle torsional fatigue behaviors of AISI 4340 steel including crack initiation, crack propagation, and fatigue life were studied in this work. Based on the experimental results and discussion, the main conclusions are summarized as follows: 1) The PFZ around the LB in the maximum shear stress plane would crack in mode II. The packet is anisotropic due to its lamellar structure and the strength in the lath direction is lower. Furthermore, the strength of PFZ around the LB is lower than the lath. 2) The MnS inclusions would crack during the cyclic loading. However, the LB vertical to the crack would prevent

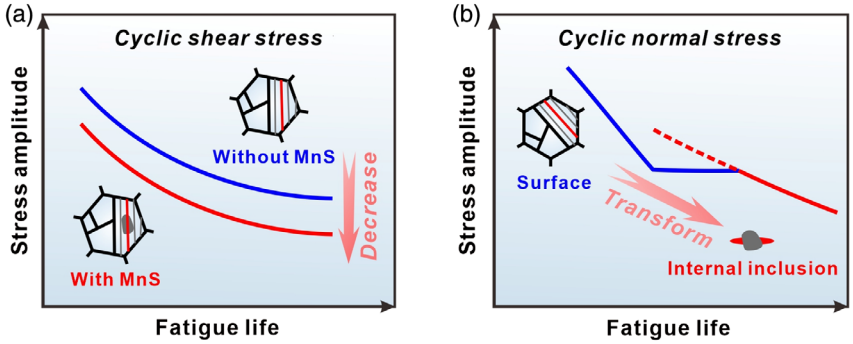

Figure 11. Schematic illustration of the effect of inclusion on the S-N curve of a) cyclic shear stress and b) cyclic normal stress.[44]

the crack from propagating into the matrix. Therefore, for mode II crack, the LB acts as a barrier when the crack is vertical to it, but as a weak region when the crack is along it. 3) The initiated crack plane usually is the maximum shear stress plane in pure torsional fatigue. However, the MnS inclusions would cause stress concentration so that LB deviating from the maximum shear stress plane could have sufficient driving force to initiate cracks. The maximum deviation angle is related to the stress concentration factor of MnS inclusion.

Acknowledgements

This work was financially supported by National Natural Science Foundation of China (NSFC) under Grant Nos. 52001310 and 52130002, the National Science and Technology Major Project of China under Grant No. J2019-VI-0019-0134, IMR Innovation Fund under Grant No. 2022-PY06, and the Special Fund Project of High-tech Industrialization Cooperation between Jilin Province and CAS under Grant Nos. 2020SYHZ0008 and 2021SYHZ0046, and the Open Research Fund from the State Key Laboratory of Rolling and Automation, Northeastern University under Grant No. 2021RALKFKT004.

Conflict of Interest

The authors declare no conflict of interest.

Data Availability Statement

The data that support the findings of this study are available from the corresponding author upon reasonable request.

Keywords

AISI 4340 steels, crack initiations, high-cycle torsional fatigues, inclusions, lath martensite

Received: December 27, 2022
Revised: March 1, 2023
Published online:

[1] Y. Tomita, *Mater. Sci. Technol.* **1991**, *7*, 481.
[2] T. Demir, M. Ubeyli, R. O. Yildirim, *J. Mater. Eng. Perform.* **2009**, *18*, 145.
[3] U. Zerbst, M. Madia, C. Klinger, D. Bettge, Y. Murakami, *Eng. Fail. Anal.* **2019**, *98*, 228.
[4] W. M. Garrison, *JOM* **1990**, *42*, 20.
[5] T. Abe, Y. Furuya, S. Matsuoka, *Tetsu To Hagane* **2003**, *89*, 711.
[6] Y. Murakami, *JSME Int. J.* **1989**, *32*, 167.
[7] D. Spriestersbach, P. Grad, E. Kerscher, *Int. J. Fatigue* **2014**, *64*, 114.
[8] P. Wang, B. Wang, Y. Liu, P. Zhang, Y. K. Luan, D. Z. Li, Z. F. Zhang, *Scr. Mater.* **2022**, *206*, 114232.
[9] Y. Murakami, in *Metal Fatigue: Effects Of Small Defects And Nonmetallic Inclusions*, Elsevier, Oxford, UK, **2002**.
[10] Y. B. Liu, Z. G. Yang, Y. D. Li, S. M. Chen, S. X. Li, W. J. Hui, Y. Q. Weng, *Mater. Sci. Eng. A* **2009**, *517*, 180.
[11] M. L. Zhu, L. Jin, F. Z. Xuan, *Acta Mater.* **2018**, *157*, 259.
[12] K. Koschella, U. Krupp, *Int. J. Fatigue* **2019**, *124*, 113.
[13] Y. Mine, K. Hirashita, H. Takashima, M. Matsuda, K. Takashima, *Mater. Sci. Eng. A* **2013**, *560*, 535.
[14] L. Morsdorf, O. Jeannin, D. Barbier, M. Mitsuhara, D. Raabe, C. C. Tasan, *Acta Mater.* **2016**, *121*, 202.
[15] G. Seidametova, J.-B. Vogt, I. Proriol Serre, *Int. J. Fatigue* **2018**, *106*, 38.
[16] M. N. Batista, M. C. Marinelli, S. Herenu, I. Alvarez-Armas, *Int. J. Fatigue* **2015**, *72*, 75.
[17] K. Okada, A. Shibata, Y. Takeda, N. Tsuji, *Int. J. Fatigue* **2021**, *143*, 105921.
[18] B. M. Schönbauer, K. Yanase, M. Chehrehrazi, M. Endo, H. Mayer, *Mater. Sci. Eng. A* **2021**, *801*, 140481.
[19] J. X. Xu, R. H. Li, P. Zhang, Z. F. Zhang, *Int. J. Fatigue* **2020**, *131*, 105304.
[20] R. H. Li, P. Zhang, Z. F. Zhang, *Mater. Sci. Eng. A* **2013**, *574*, 113.
[21] I. Serrano-Munoz, D. Shiozawa, S. Dancette, C. Verdu, J. Y. Buffiere, *Acta Mater.* **2020**, *201*, 435.
[22] B. Wang, Q. Q. Duan, P. Zhang, Z. J. Zhang, X. W. Li, Z. F. Zhang, *Mater. Sci. Eng. A* **2020**, *771*, 138553.
[23] B. Wang, P. Zhang, Q. Q. Duan, Z. J. Zhang, H. J. Yang, X. W. Li, Z. F. Zhang, *Mater. Sci. Eng. A* **2017**, *707*, 674.
[24] Z. K. Xu, B. Wang, P. Zhang, Z. F. Zhang, *Mater. Sci. Eng. A* **2021**, *807*, 140844.
[25] Z. K. Xu, B. Wang, P. Zhang, Z. F. Zhang, *Mater. Sci. Eng. A* **2020**, *789*, 139659.
[26] C. W. Huang, Y. Q. Zhao, S. W. Xin, C. S. Tan, W. Zhou, Q. Li, W. D. Zeng, *Mater. Sci. Eng. A* **2017**, *682*, 107.
[27] C. W. Huang, Y. Q. Zhao, S. W. Xin, C. S. Tan, W. Zhou, Q. Li, W. D. Zeng, *Int. J. Fatigue* **2017**, *94*, 30.
[28] G. Lütjering, J. Albrecht, C. Sauer, T. Krull, *Mater. Sci. Eng. A* **2007**, *468–470*, 201.
[29] J. Monnot, B. Heritier, J. Y. Cogne, *ASTM STP* **1988**, *987*, 149.
[30] S. X. Li, *Int. Mater. Rev.* **2012**, *57*, 92.
[31] M. D. Sangid, *Int. J. Fatigue* **2013**, *57*, 58.
[32] K. Differt, U. Essmann, H. Mughrabi, *Philos. Mag. A* **1986**, *54*, 237.
[33] U. Essmann, U. Gosele, H. Mughrabi, *Philos. Mag. A* **1981**, *44*, 405.
[34] M. Herbig, A. King, P. Reischig, H. Proudhon, E. M. Lauridsen, J. Marrow, J.-Y. Buffière, W. Ludwig, *Acta Mater.* **2011**, *59*, 590.
[35] S. Suresh, in *Fatigue Of Materials*, Cambridge University Press, Cambridge, UK, **1998**.
[36] M. A. Meyers, K. K. Chawla, in *Mechanical Behavior Of Materials*, Cambridge university press, Cambridge, UK, **2008**.
[37] K. Tanaka, T. Mura, *J. Appl. Mech.* **1981**, *48*, 97.
[38] T. Mura, Y. Nakasone, *J. Appl. Mech.* **1990**, *57*, 1.
[39] K. S. Chan, *Metall. Mater. Trans. A* **2003**, *34*, 43.
[40] Y. Murakami, S. Kodama, S. Konuma, *Int. J. Fatigue* **1989**, *11*, 291.
[41] Z. K. Xu, B. Wang, P. Zhang, X. Z. Gu, Z. F. Zhang, *Mater. Sci. Eng. A* **2023**, *863*, 144561.
[42] D. Jeddi, T. Palin-Luc, *Fatigue Fract. Eng. Mater. Struct.* **2018**, *41*, 969.
[43] K. Shiozawa, L. Lu, S. Ishihara, *Fatigue Fract. Eng. Mater. Struct.* **2001**, *24*, 781.
[44] T. Sakai, Y. Sato, N. Oguma, *Fatigue Fract. Eng. Mater. Struct.* **2002**, *25*, 765.